Supporting Information for

Tailoring Sapphire–Invar Welds Using Burst Femtosecond Laser

Xianshi Jia [1], Yuyang Chen [1], Zhaoxi Yi [1], Jiawei Lin [1], Jinlin Luo [1], Kai Li [1], Cong Wang [1*], Ji'an Duan [1], D. S. Polyakov [2], V. P. Veiko [2]

[1]Central South University, College of Mechanical and Electrical Engineering, State Key Laboratory of Precision Manufacturing for Extreme Service Performance, Changsha, China, 410083

[2]Institute of Laser Technologies, ITMO University, Saint-Petersburg, Russia

**Corresponding author, wangcong@csu.edu.cn (C. Wang)*

Supplementary S1. Sample morphology and surface roughness

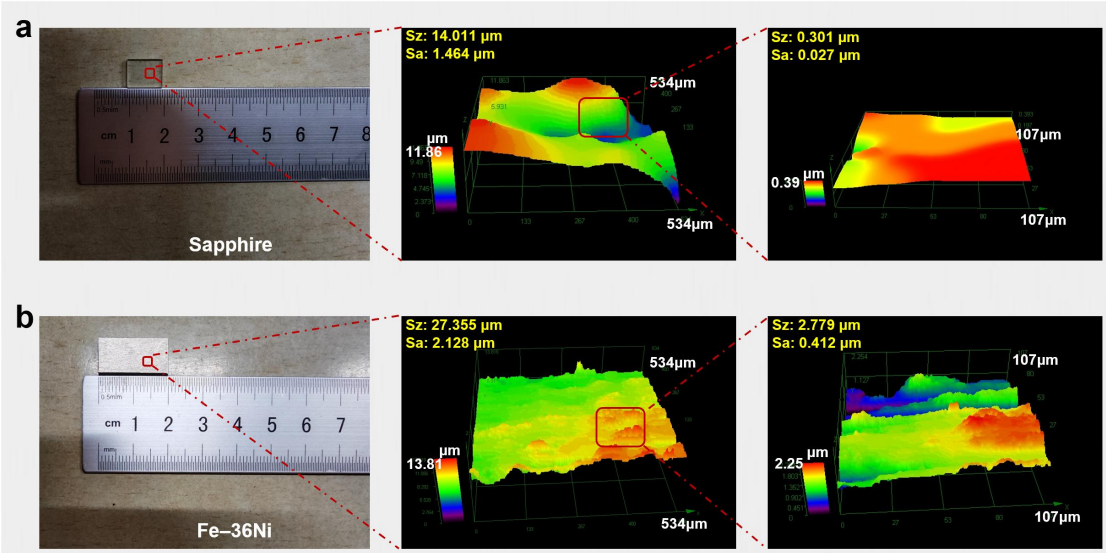

Figure S1. Samples used for welding: (a) sapphire and (b) Invar alloy. Within a measurement area of 534 μm in length and width, the surface roughness of the sapphire exhibited a Sa value of 1.464 μm and an Sz value of 14.011 μm, and the Invar alloy exhibited a Sa value of 2.128 μm and an Sz value of 27.355 μm. Within a measurement area of 107 μm in length and width, the surface roughness of the sapphire exhibited a Sa value of 0.027 μm and an Sz value of 0.301 μm, and the Invar alloy exhibited a Sa value of 0.412 μm and an Sz value of 2.799 μm.

Supplementary S2. High-speed Plasma Imaging System and Image Processing

A high-speed plasma imaging system was established to capture the dynamic behaviour at a heterogeneous interface during femtosecond laser welding. The system employed a 10× objective lens to observe the laser interaction region, where the interface-emitted plasma was recorded using a high-speed camera (FASTCAM NOVA S9; Photron, Japan), as shown in **Fig. S2**. The system achieved a spatial resolution better than 2 μm and temporal resolution of 0.11 ms at a frame rate of 9000 frames per second. The exposure time of the high-speed camera is 1.1 μs, indicating that the obtained plasma image represents an averaged effect over this duration.

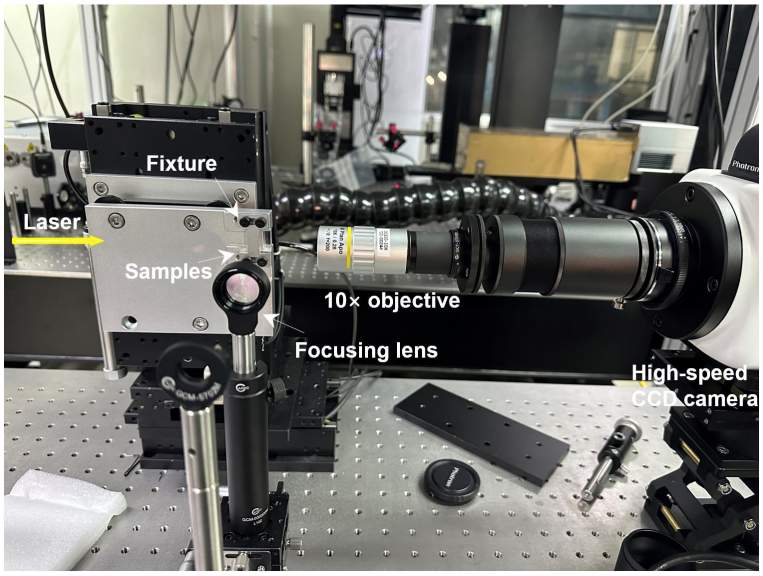

Figure S2. Photograph of high-speed camera imaging setup for femtosecond laser welding region.

To obtain clearer images, the original greyscale images were converted into colour images using MATLAB, as shown in **Fig. S3**. Specifically, **Figs. S3b** and **S3d** were derived from **Figs. S3a** and **S3c**, respectively). The original images were single-channel grayscale images with a brightness range of 0–4095, where 0 represents the darkest pixel and 4095 represents the brightest pixel. The brightness of the original images was read using MATLAB, and the brightness data were normalised to values between 0 and 1. Finally, the brightness values between 0 and 1 were mapped to MATLAB's built-in colormap “jet”, thus obtaining the processed colour images. The colour bar on the right of each image serves as a legend, indicating the mapping relationship between the

brightness values and colours.

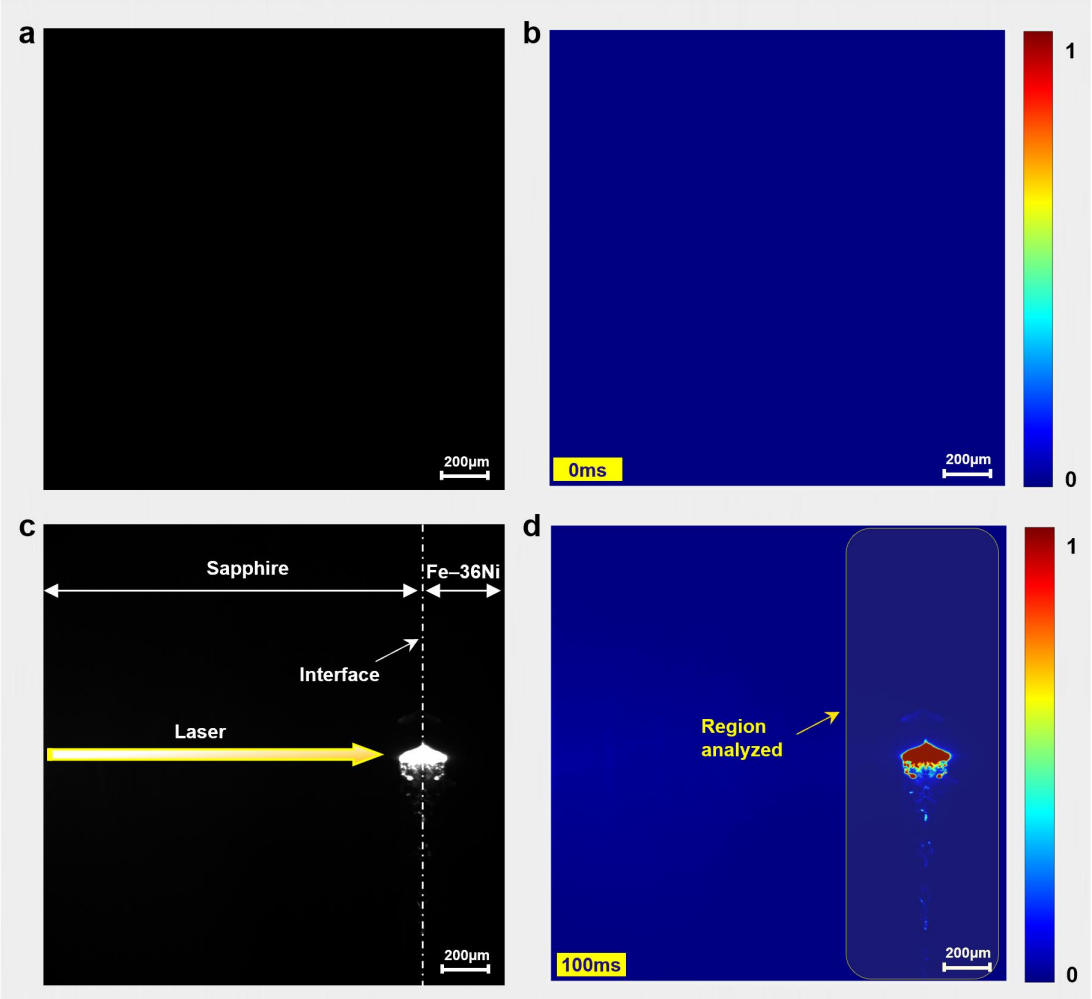

Figure S3. Grayscale images and corresponding color images. (a) Background image, **(b)** converted background image, **(c)** transient images captured during the welding process, and **(d)** converted image.

In addition, due to the opacity of Invar alloy, the internal plasma could not be effectively captured by the high-speed camera. Moreover, because of the high brightness of the plasma and high reflectivity of the metal surface, the plasma images recorded by the CCD appeared symmetrically along the heterogeneous interface (**Fig. S3C**). Therefore, in the following analysis, we primarily focus on the plasma morphology within the sapphire above the interface, including its brightness (representing the plasma density) and spatial distribution.

Supplementary S3. Cross-sections and surfaces of joints after femtosecond laser welding under different modes.

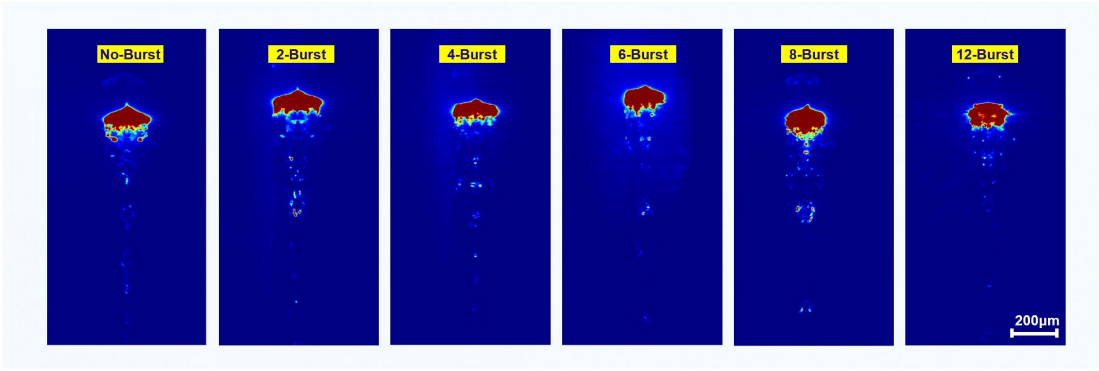

Figure S4. Plasma images after the femtosecond laser welding reaches steady state under different modes.

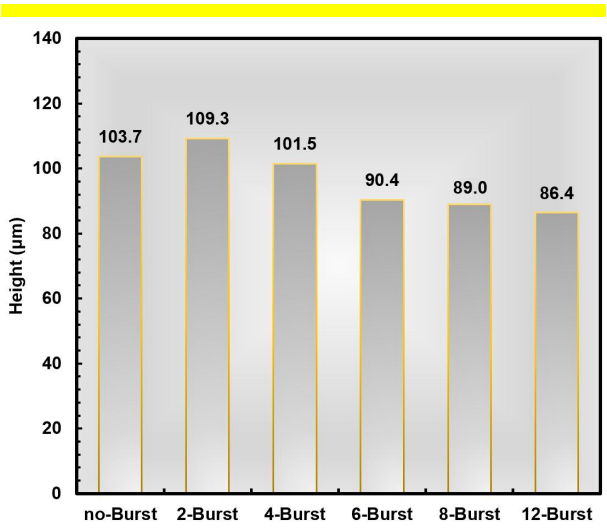

Figure S5. Plasma height data formed during the femtosecond laser welding process under different modes.

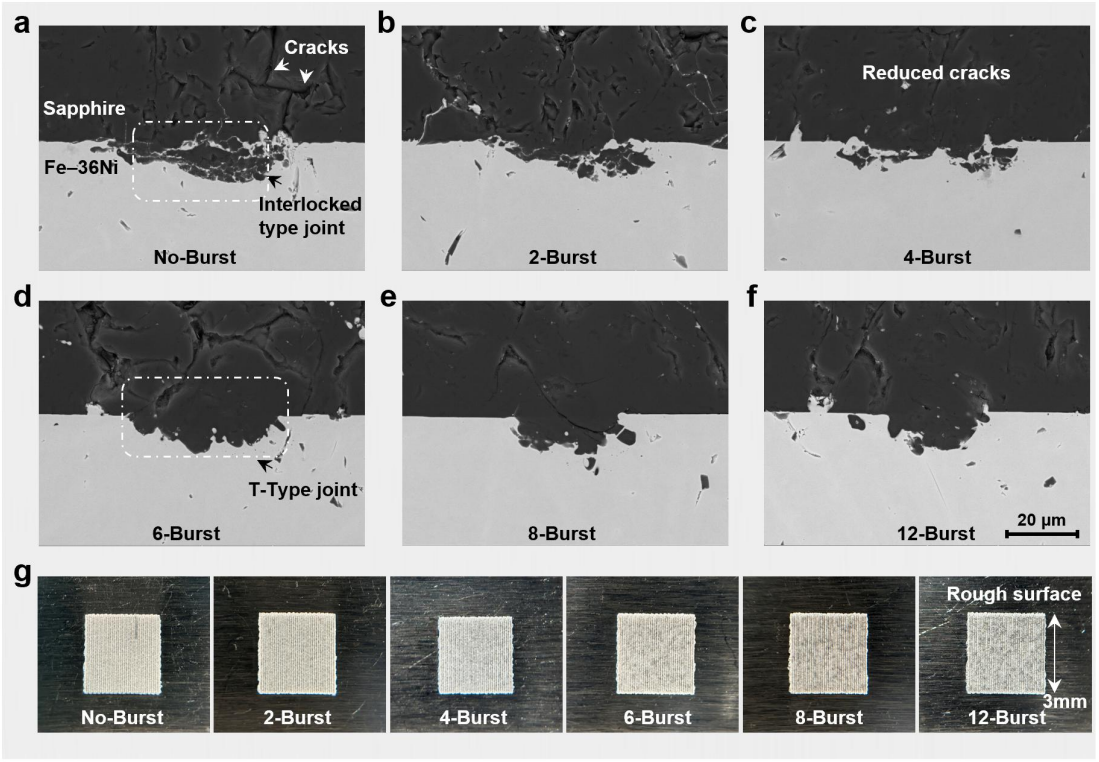

Figure S6. Joint morphology of Invar alloy-sapphire femtosecond laser welding. (a)–(f) represented the joint cross-sectional morphology of femtosecond laser welding under non-Burst, 2-Burst, 4-Burst, 6-Burst, 8-Burst, and 12-Burst modes, respectively. **(g)** Corresponding weld surface morphology.

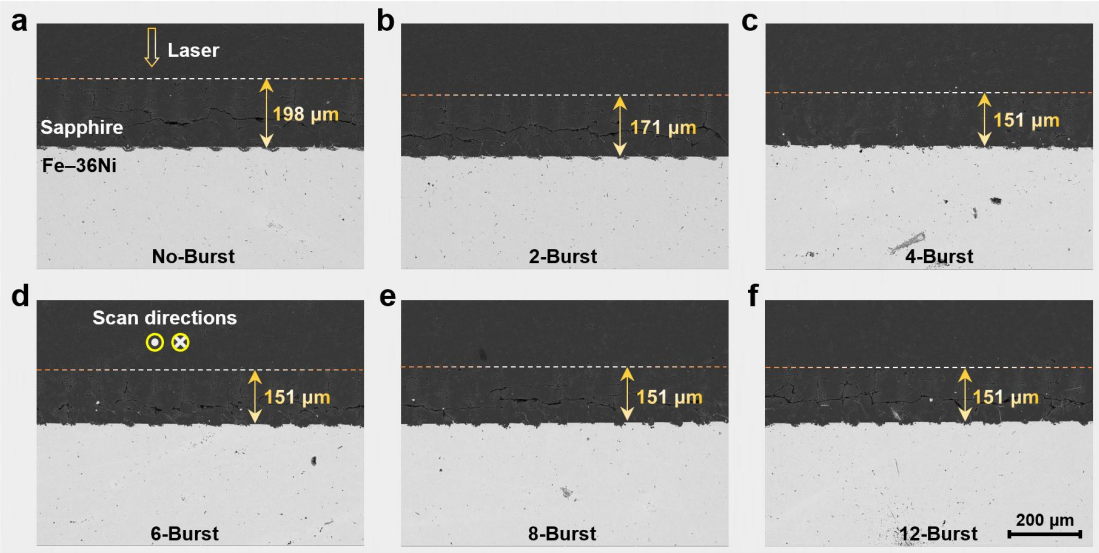

Figure S7. Modification depth inside sapphire after femtosecond laser welding under different modes.

Supplementary S4. Analysis of time-resolved plasma imaging during femtosecond laser welding

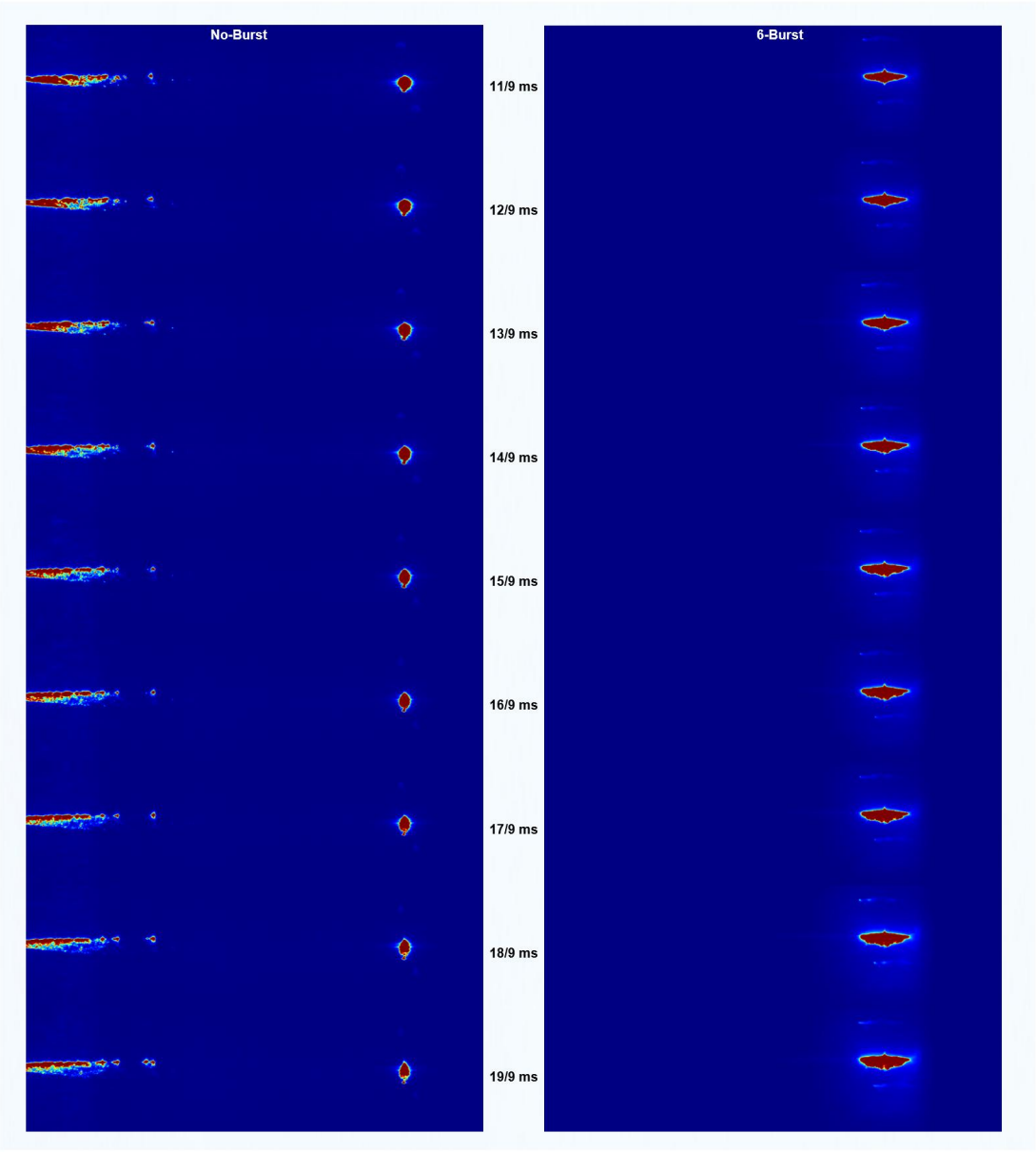

Figure S8. Comparison of the femtosecond laser energy deposition and melting process of the transparent material under two different modes.

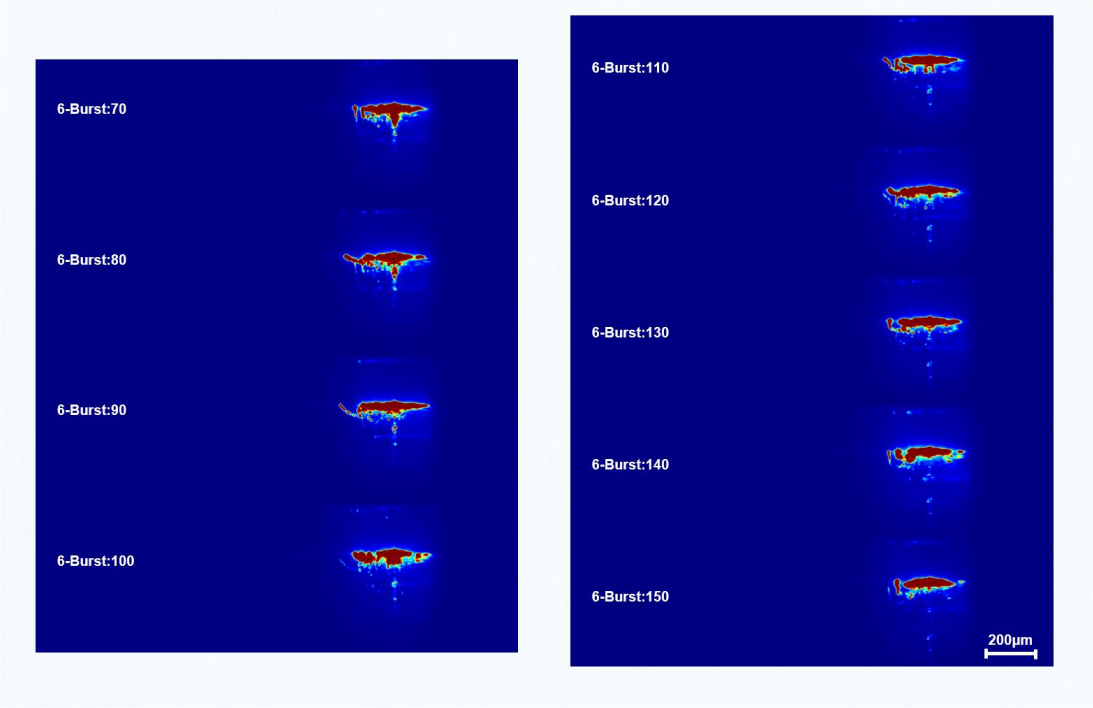

Figure S9. Dynamic evolution of laser energy coupling between linear and nonlinear absorption during the femtosecond laser welding process.

Supplementary S5. Interfacial morphology and elemental distribution of the joints welded using femtosecond lasers in different modes.

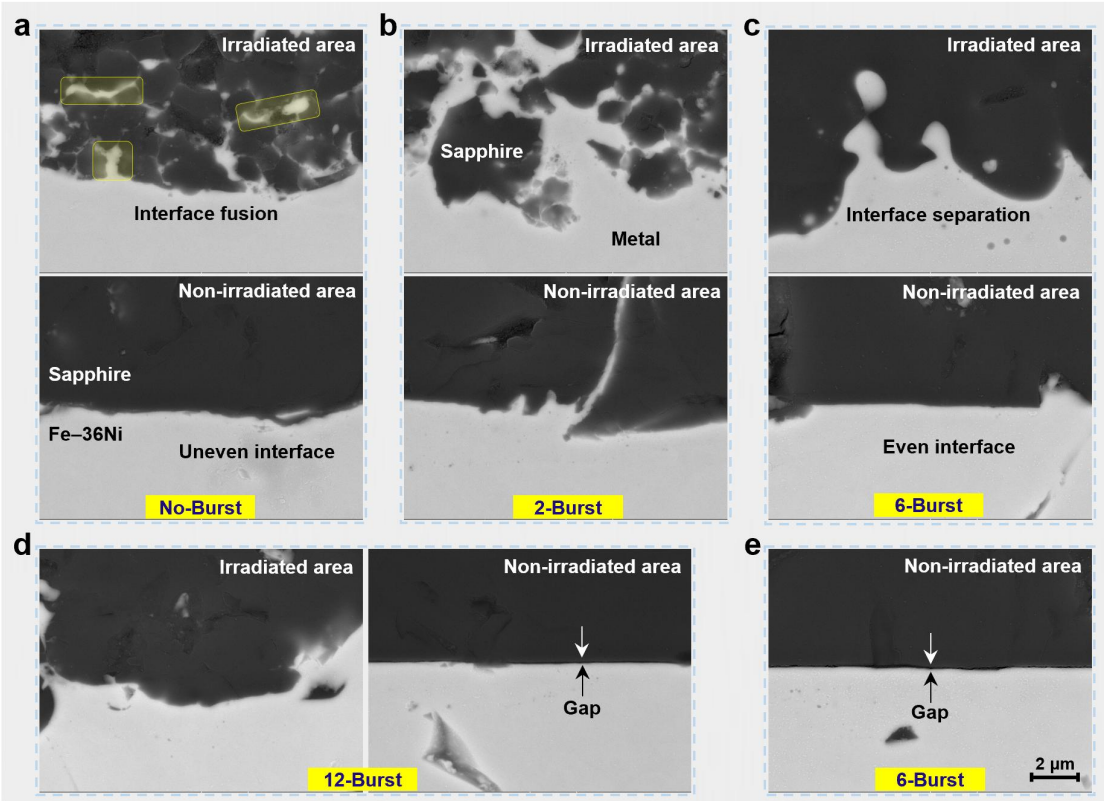

Figure S10. Results of interfacial composition integration in sapphire-Invar alloy welded joints. The interfacial morphology in the laser-irradiated and non-irradiated regions under the **(a)** non-Burst mode, **(b)** 2-Burst mode, **(c)** 6-Burst mode, and **(d)** 12-Burst mode. **(e)** Interfacial air gap detected in the femtosecond laser welding area under the 6-Burst mode.

.

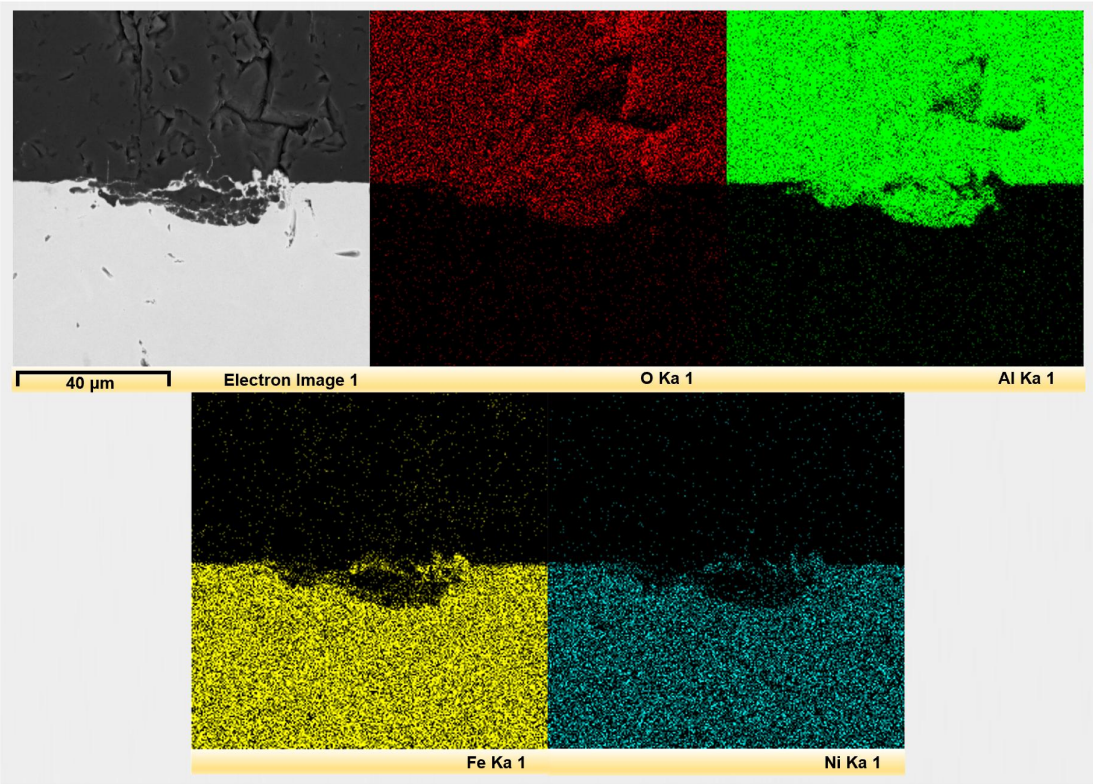

Figure S11. Interfacial element distribution in the femtosecond laser welded joints under the non-Burst mode.

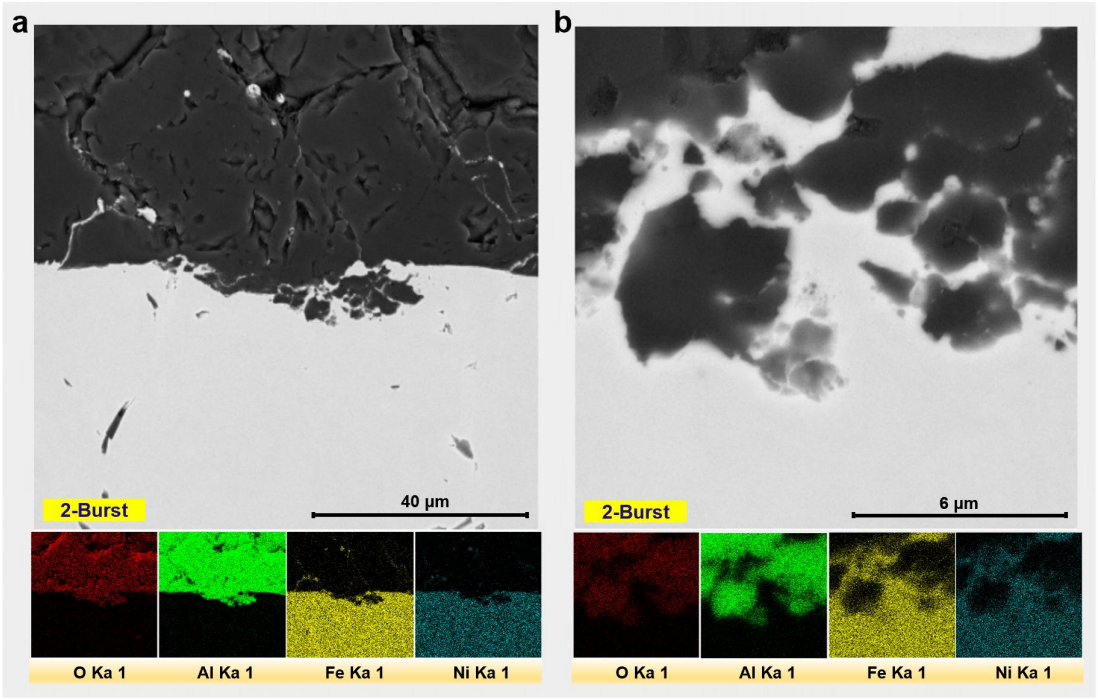

Figure S12. Interfacial element distribution in the femtosecond laser welded joints under the 2-Burst mode.

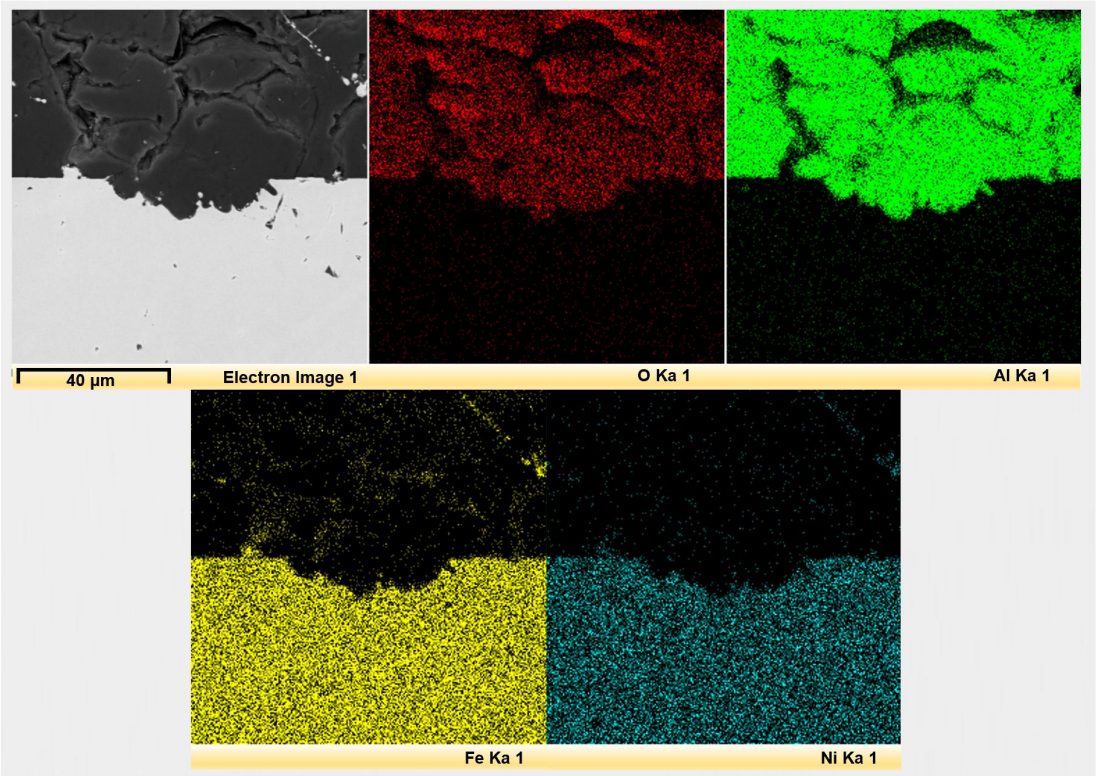

Figure S13. Interfacial element distribution in the femtosecond laser welded joints under the 6-Burst mode.

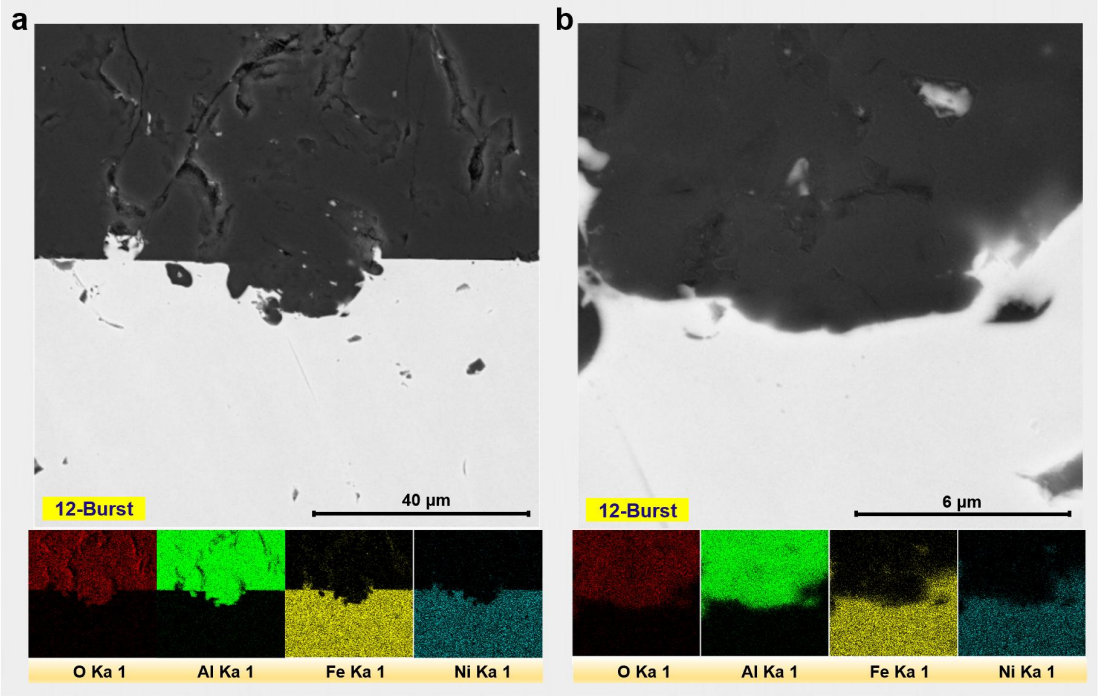

Figure S14. Interfacial element distribution in the femtosecond laser welded joints under the 12-Burst mode.

Supplementary S6. Welding strength results obtained under different femtosecond laser modes.

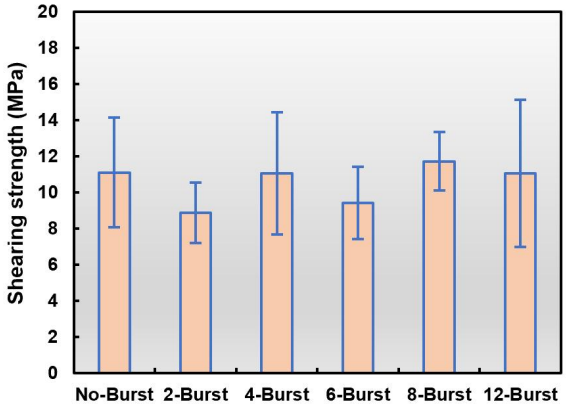

Figure S15. Welding strength under different mode femtosecond laser welding.

Supplementary S7. Factors influencing welding strength under different femtosecond laser modes.

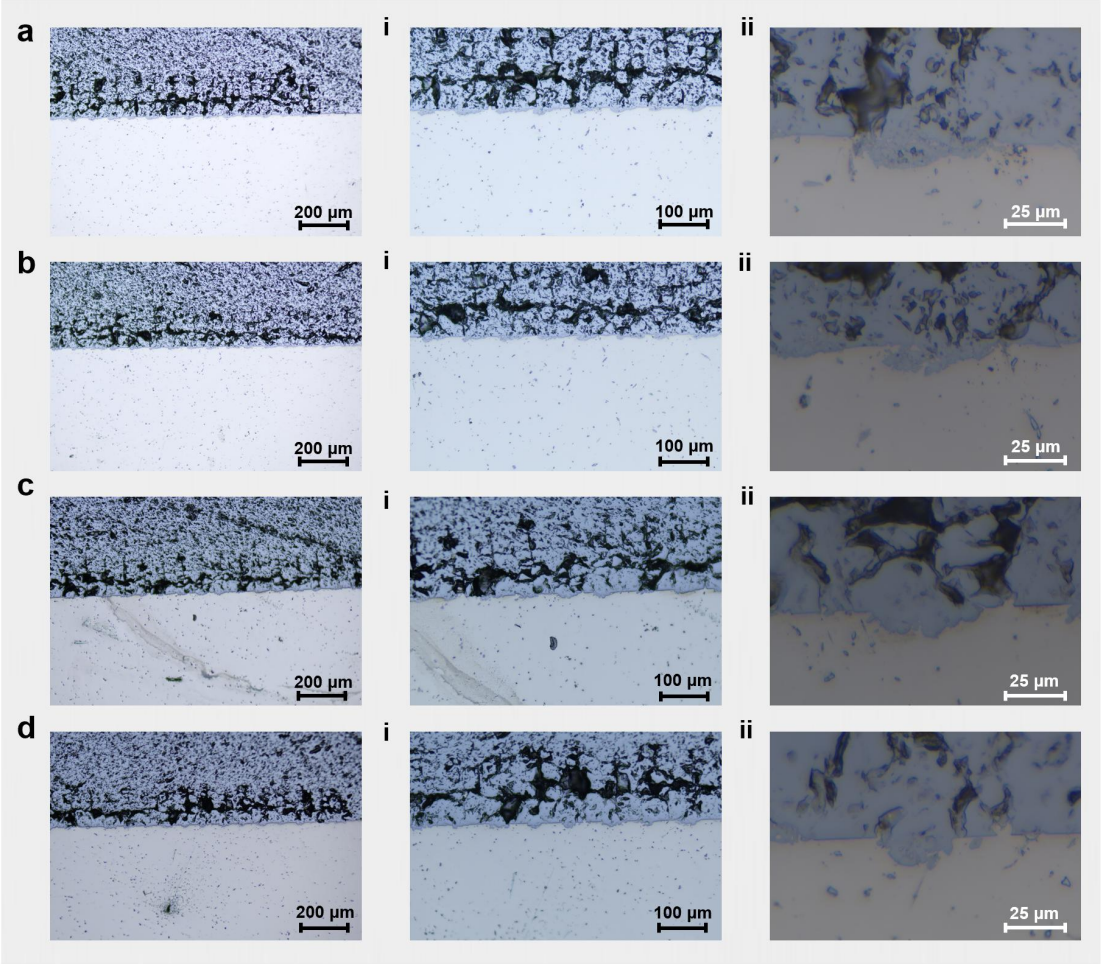

Figure S16. Joint cross-sectional morphology measured under the reflection mode of the optical microscope. (a) non-Burst mode, **(b)** 2-Burst mode, **(c)** 6-Burst mode, and **(d)** 12-Burst mode.

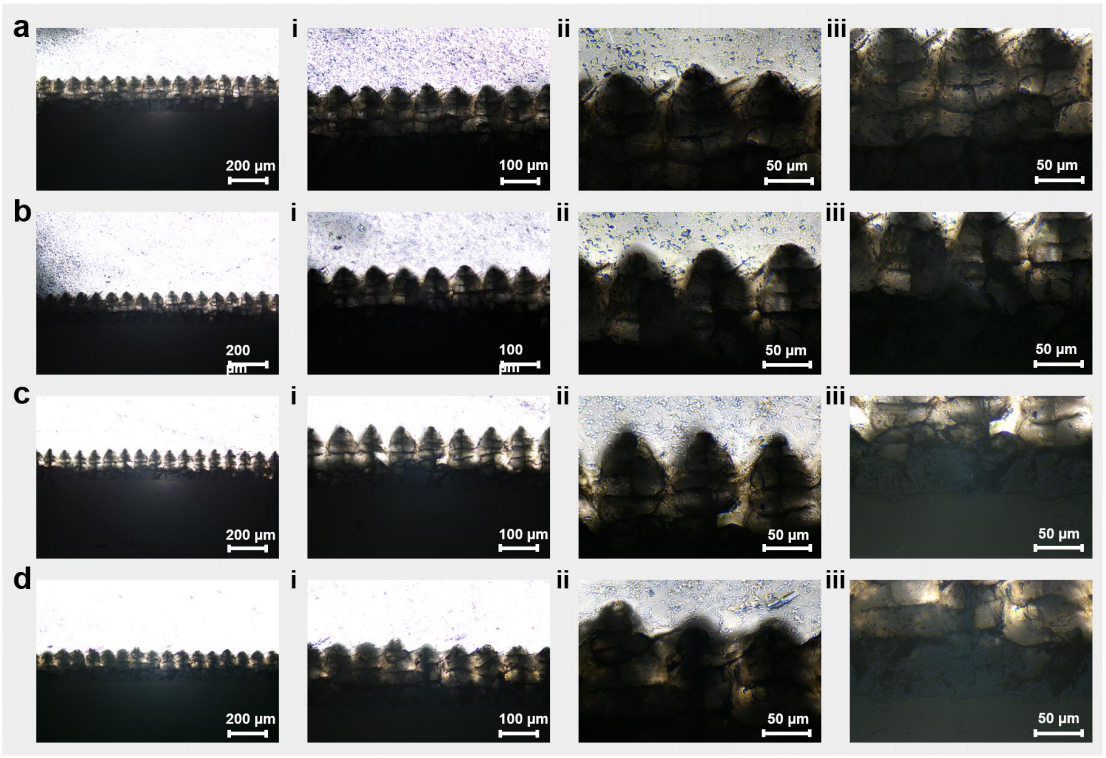

Figure S17. Joint cross-sectional morphology measured under the transmission mode of the optical microscope. (a) non-Burst mode, **(b)** 2-Burst mode, **(c)** 6-Burst mode, and **(d)** 12-Burst mode.

Supplementary S8. Clamping fixture used in the welding experiments.

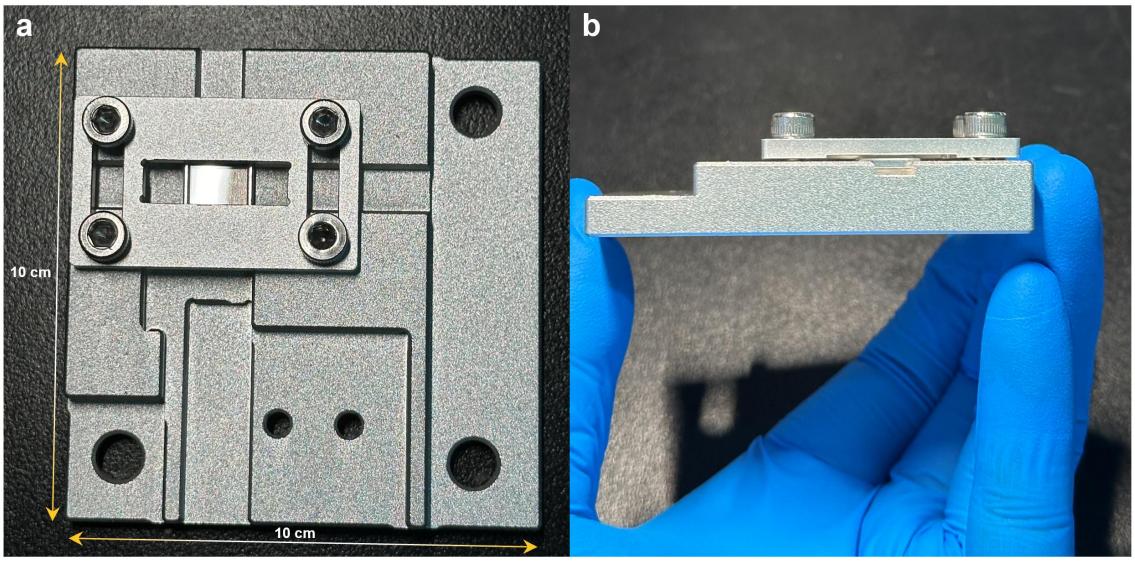

Figure S18. Clamping fixture. (a) Top view, and **(b)** side view.